nature methods

BRIEF COMMUNICATION

https://doi.org/10.1038/s41592-019-0728-9

Simultaneous multiplane imaging with reverberation two-photon microscopy

Devin R. Beaulieu[1*], Ian G. Davison[2,3], Kıvılcım Kılıç[4], Thomas G. Bifano[3] and Jerome Mertz[3,4]

Multiphoton microscopy has gained enormous popularity because of its unique capacity to provide high-resolution images from deep within scattering tissue. Here, we demonstrate video-rate multiplane imaging with two-photon microscopy by performing near-instantaneous axial scanning while maintaining three-dimensional micrometer-scale resolution. Our technique, termed reverberation microscopy, enables the monitoring of neuronal populations over large depth ranges and can be implemented as a simple add-on to a conventional design.

Many brain areas, such as the neocortex[1] and olfactory bulb[2], are vertically organized into layers containing distinct cell types that have different activity profiles and that project to different downstream targets. Fast imaging over large depths is thus indispensable for capturing the dynamics of neuronal populations within their stratified environments. The standard method for imaging over volumes with multiphoton microscopy (MPM) is to perform x–y scanning with galvanometric mirrors, and then z scanning by adjusting the microscope objective; this is slow and cumbersome[3].

Faster imaging can be done by purposefully decreasing image resolution[4], or by using faster z-scanning mechanisms, such as electrically tunable lenses[5], deformable mirrors[6], voice coils[7] or tunable acoustic gradient (TAG) lenses[8]. For example, TAG can provide axial scan rates at tens of kilohertz, though at the cost of limited depth range. Alternatively, simultaneous multifocus[9] extended focus[10] or stereoscopic[11] illumination can be achieved by wavefront engineering, providing two-dimensional (2D) images of volumetric samples obtained from single transverse scans. While fast, these solutions sacrifice axial resolution by yielding only 2D projections. Axial localization and segmentation can be calculated post acquisition, but with the requirement of computational models and/or a priori knowledge about the sample structure. Consequently, such solutions involving simultaneous spatially multiplexed illumination are best suited for sparse samples.

The use of high-speed detection electronics has opened new approaches for near-simultaneous temporal multiplexing, by taking advantage of the ability of these instruments to individually measure fluorescence signals a few nanoseconds apart. This has been implemented in previous work by separating the illumination beam into a few (up to four) beamlets of different pathlengths[12–16], in which the signals produced by each beamlet are distinguished in time using fast-detection electronics. By focusing each beamlet to a different depth within the sample, a few planes can be obtained near simultaneously from a single transverse scan. However, such spatiotemporal multiplexing becomes technically cumbersome as the number of beamlets increases, and leads to laser power loss when the number of beamlets is greater than two (unless the focal planes are staggered in the transverse direction[12,13,16]). Similar spatiotemporal multiplexing approaches have been reported for fast transverse scanning[17], as well as camera-based imaging[18].

We present here a simplified implementation of spatiotemporal multiplexing that provides an infinite series of vertically distributed beam foci, performing a near-instantaneous axial scan, with essentially no loss in laser power. Our system makes use of reverberation loop upstream of the beam steering mirrors (Fig. 1a). A 50/50 nonpolarizing beamsplitter divides the illumination beam, with one-half of the light proceeding to the sample normally, and one-half entering the loop. The loop's unit-magnification relay lens pair is intentionally misadjusted (its lenses spaced too far apart), causing a shift in the beam focus. Upon returning to the beamsplitter, half of the light exits the loop and proceeds to the sample, but it is focused to a shallower depth in the sample (a shift of Δz) and time delayed (owing to the time spent in the loop). The light remaining in the loop continuously repeats the process, accumulating an increasing focal shift and time delay upon each pass.

Each laser pulse entering the reverberation loop thus produces a series of beam foci of decreasing depth within the sample that arrive sequentially in time. The incident power associated with the n-th focal spot is given by $P_n = 2^{-(n+1)} \times P_{in}$, where P_{in} is the total laser power incident on the loop and $n = 0$ corresponds to the deepest plane in the sample. In MPM, only the ballistic (that is, unscattered) portion of this power contributes to fluorescence generation[3]. The relative fluorescence power produced at each focal spot is thus given by $F_n = F_0 \exp[mn(\Delta z/l_s - \ln(2))]$, where m is the nonlinear order ($m = 2$ for two-photo microscopy (2PM)) and l_s is the scattering-mean-free path at the illumination wavelength, and we have assumed a roughly homogeneous fluorescence labeling density. In other words, even though the incident power associated with each focal spot decreases geometrically with decreasing depth (increasing n), the resulting fluorescence may or may not decrease depending on our choice of Δz (which can be adjusted even while actively imaging). In particular, if the inter-plane spacing is chosen such that $\Delta z = l_s \times \ln(2)$, then the decrease in scattering at shallower depths exactly compensates for the decrease in incident power with increasing n, and the fluorescence produced from each focal spot remains roughly constant at all depths. Alternatively, if a finer inter-plane spacing is desired (that is, $\Delta z < l_s \times \ln(2)$), the fluorescence becomes successively dimmer with shallower depths, which can be corrected in postprocessing, albeit with some loss in signal-to-noise ratio (Supplementary Note 1).

Figure 1b illustrates the timing of the illumination and fluorescence pulses, with a different color indicating each focal depth. A 2-m-long reverberation loop produces a 6.7-ns delay between focal depths, allowing each to be measured individually using a high-speed amplifier (400 MHz bandwidth) and digitizer (1.5 GS s^{-1}). To properly distinguish the signal from successive focal spots, the

[1]Department of Electrical Engineering, Boston University, Boston, MA, USA. [2]Department of Biology, Boston University, Boston, MA, USA. [3]Photonics Center, Boston University, Boston, MA, USA. [4]Department of Biomedical Engineering, Boston University, Boston, MA, USA. *e-mail: devinrbeaulieu@icloud.com

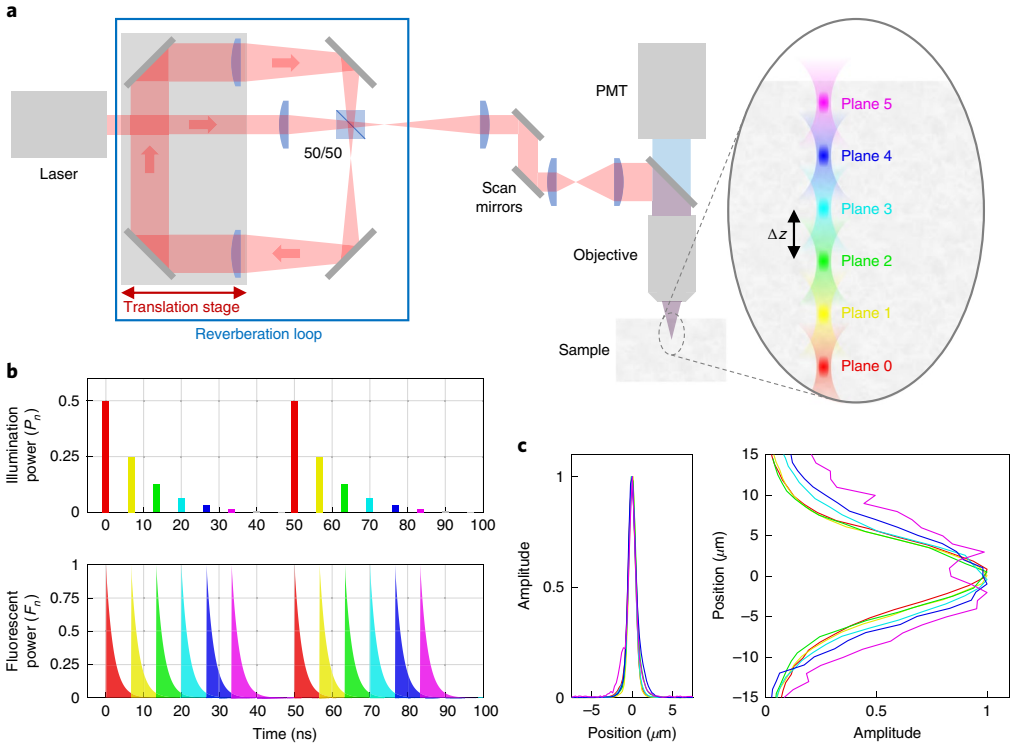

Fig. 1 | Reverberation 2PM design and characteristics. a, Schematic of microscope layout. For each input laser pulse, the reverberation loop creates an infinite series of beam foci separated in space and time, with fluorescence naturally terminating at the sample surface after plane 5. The spatial separation (Δz) between foci is controlled (even during imaging) by adjusting the path length of the loop with a translation stage. (See Supplementary Note 1 for further design information.) **b**, Timing and power of illumination pulses and corresponding fluorescence signals (using, for example, a 4-ns fluorescence lifetime). Here Δz is chosen such that all planes have comparable fluorescence (the reduction in illumination power between planes is exactly offset by the reduction in scattering from shallower foci). **c**, Transverse and axial point spread functions at each plane with Δz of 90 μm, as measured with a 0.5-μm bead.

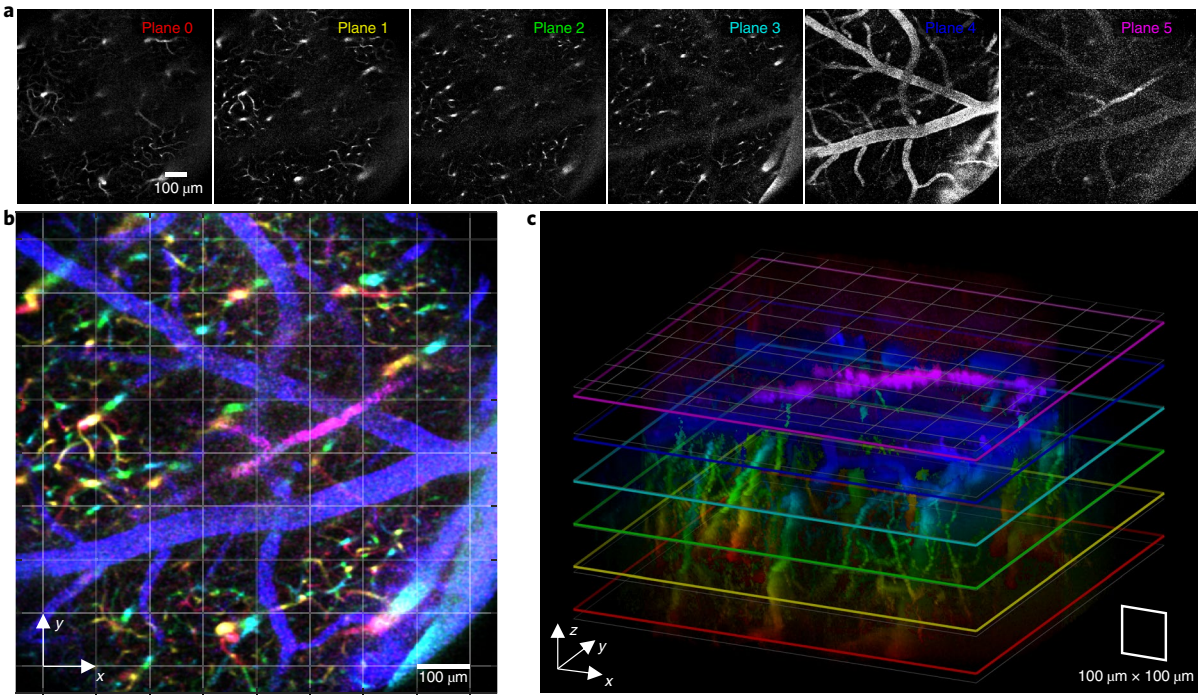

Fig. 2 | Reverberation 2PM imaging of in vivo mouse brain vasculature. a, Six independent reverberation planes at different depths from a single image with Δz of ~90 μm. **b**, Merged image comprising the six planes; color indicates plane and depth (the single color of each plane merged in overlapping regions). **c**, Maximum intensity projection of *z*-stack (using short physical *z*-scan to fill in the gaps between reverberation planes) with slices from all six reverberation planes merged into a volume; color indicates depth. (Fly-through and fly-around are provided in Supplementary Videos 1 and 2.) Planes highlighted in **c** correspond to those in **a** and **b**. All images are corrected for crosstalk.

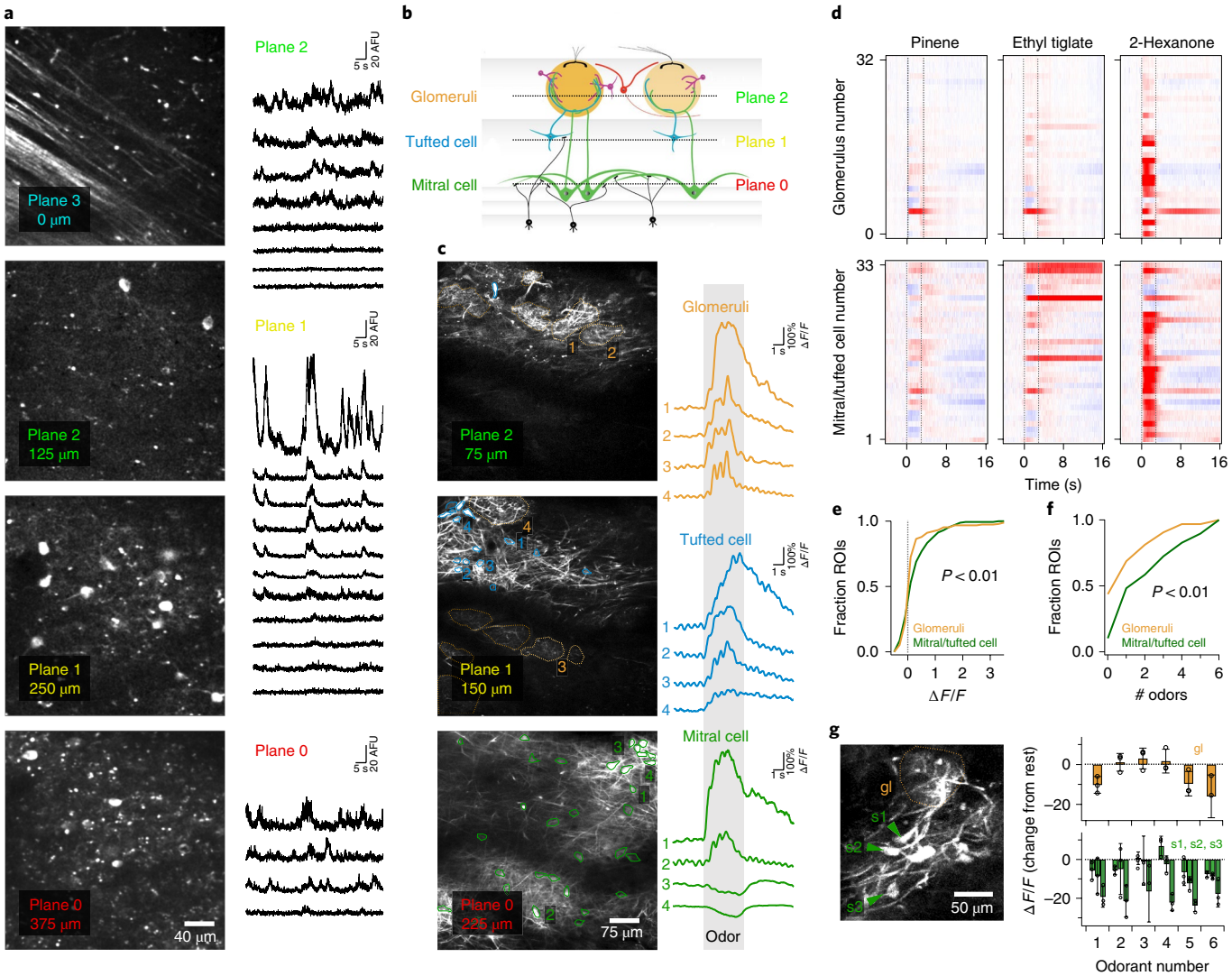

Fig. 3 | Reverberation imaging of in vivo mouse brain neural activity. a, Time-averaged *x*–*y* images of GCaMP6s-expressing neurons from four different planes of neocortex, with the top plane positioned at the brain surface (Supplementary Video 3). Traces to the right show the activity of individual neurons imaged in different sub-surface layers. **b**, Schematic showing the intersection of imaging planes with neuropil and cell types at different depths, modified from ref. [2]. **c**, Time-averaged *x*–*y* images of dendrites and somata of GCaMP6f-expressing neurons imaged in three different planes of main olfactory bulb (Supplementary Video 4). To the right, representative traces showing sensory responses to the odorant ethyl tiglate in postsynaptic dendrites (gold) and somata of two different classes of olfactory-bulb projection neurons (blue, green). **d**, Heat maps showing sensory responses in 32 glomeruli (top, containing postsynaptic dendrites) and 33 mitral/tufted somata (bottom) measured in a separate mouse (z-stack in Supplementary Video 5). Three representative odorants shown of six total. (Corresponding regions of interest (ROIs) are shown in the Supplementary Information.) **e**, Comparison of the distribution of response strengths for glomeruli (gold) and mitral/tufted cells (green). Mitral cells showed a significant shift towards stronger sensory responses ($P = 0.29 \times 10^{-3}$, two-sided Kolmogorov–Smirnov test; $n = 32$ glomeruli, 33 mitral cell somata). **f**, Comparison of odorant selectivity for glomeruli and mitral cells. On average, mitral cells responded to significantly more odorants than glomeruli ($P = 6.5 \times 10^{-3}$, two-sided Mann–Whitney test; $n = 32$ glomeruli, 33 mitral cell somata). **g**, Example of simultaneous imaging of postsynaptic dendrites (gold) and somata of three different mitral/tufted cells (green; s1, s2, s3) contained within a single glomerulus (gl). Bar plots show average response profiles across the panel of six odorants ($n = 3$ trials, error bars represent ±1 s.d.). In this example, odor responses largely caused suppression relative to resting activity levels.

time delay between these should be longer than the indicator fluorescence lifetime, which is typically a few nanoseconds. In our setup, the fluorescence signal was integrated over time bins of durations up to 6.7 ns, corresponding to the reverberation delay, allowing us to capture most of the fluorescence produced by each focal spot while maintaining a small crosstalk of typically less than 9% between successive spots. We note that most of this crosstalk can be removed in postprocessing, by subtracting a proportion of the previous plane from each plane (Supplementary Note 1). In theory, the pulse reverberation subsists indefinitely (with decreasing power), producing an arbitrary number of focal depths. In practice, the fluorescence naturally terminates at n when the $(n + 1)$-th focal spot exits the sample, thus preventing it from overlapping with signals from the following laser pulse.

The dual constraints of maximizing the number of planes between laser pulses while minimizing inter-plane fluorescence crosstalk motivate the use of lasers with slower repetition rates and correspondingly higher pulse powers. As it happens, such lasers are advantageous for deep imaging[19], and even indispensable for three-photon imaging[20]. To achieve a lower repetition rate with our standard 80-MHz laser, we used an electro-optic pulse picker to select every fourth pulse (Methods) and obtained an effective repetition

rate of 20 MHz (50-ns period), but we still could deliver a maximum total power of about 100 mW to the sample. We further verified that our microscope provides 3D micrometer-scale resolution, similar to a conventional MPM, by measuring the transverse and axial responses, and showing that these are not substantially modified between planes (Fig. 1c and Supplementary Note 1).

To demonstrate the effectiveness of reverberation 2PM for biological imaging, we performed in vivo imaging of mouse brain vasculature labeled with FITC–dextran (Fig. 2). In this experiment, l_s was found to be approximately 200 µm for an excitation wavelength of 940 nm, and the planes were spaced 92 µm apart. These results illustrate our capacity to obtain a comprehensive snapshot of brain tissue over an extended depth range, acquired as multiple independent, optically sectioned planes spanning large fields of view (here up to 900 µm).

Finally, we performed Ca^{2+} imaging of GCaMP6-labeled neurons in the mouse motor cortex and olfactory bulb (Fig. 3a–d). Both resting activity and sensory-driven responses were clearly visible across several imaging planes, illustrating our ability to simultaneously monitor neural activity over multiple cell layers. We used reverberation 2PM to compare sensory tuning in the cell bodies of projection neurons in deeper layers, whose activity reflects olfactory bulb output, with responses in superficial layers where the dendrites of these neurons receive their sensory input. We observed transformations of sensory responses between dendrites and soma, including varying responses across different cells receiving the same presynaptic input (Fig. 3e–h). Odor tuning of somatic responses was broadly similar, but not identical to, that of the parent glomerulus, and responses also varied across the three neurons. The multiplane imaging rate provided by our microscope is limited by the speed of our transverse x–y scanning, which here is video-rate (30 Hz) and thus amply sufficient to monitor even the fastest GCaMP6 dynamics.

While this demonstration focused specifically on reverberation 2PM, our technique can be applied more generally to MPM. Reverberation MPM presents many advantages for multiplane imaging deep into scattering tissue, with few drawbacks. In particular, it benefits from the power efficiency that naturally comes from stacking planes in the axial, rather than transverse, direction (Supplementary Note 1). The same laser power that produces only two planes when transversely distributed can produce many more planes when axially distributed, starting from equal depth and extending all the way to the sample surface. To achieve the same maximum depth penetration as a standard MPM, all that is required is a doubling of overall laser power delivered to the sample, independent of the number of planes. Alternatively, for the same laser power delivered to the sample, the small price paid is a reduction in the maximum attainable depth penetration by an amount Δz. For the imaging results presented here, our use of a pulse picker caused our laser power to be weaker than typically used in mouse brain experiments; nevertheless, we were able to achieve simultaneous probing of fluorescence throughout a depth range of ~500 µm. In the future, reverberation MPM can provide a strong advantage for ultra-deep imaging with low-repetition-rate lasers that do not require pulse pickers, as used, for example, in three-photon microscopy. Reverberation MPM is both light efficient and simple to implement, and requires only the addition of a reverberation loop to a conventional MPM equipped with fast detection electronics. These advantages make it particularly attractive as a general technique for fast, high-resolution, large-scale multiplane imaging in scattering media.

Online content

Any methods, additional references, Nature Research reporting summaries, source data, extended data, supplementary information, acknowledgements, peer review information; details of author contributions and competing interests; and statements of data and code availability are available at https://doi.org/10.1038/s41592-019-0728-9.

Received: 1 January 2019; Accepted: 19 December 2019;
Published online: 10 February 2020

References

1. Adesnik, H. & Naka, A. Cracking the function of layers in the sensory cortex. *Neuron* **100**, 1028–1043 (2018).
2. Nagayama, S., Homma, R. & Imamura, F. Neuronal organization of olfactory bulb circuits. *Front. Neural Circuits* **8**, 98 (2014).
3. Helmchen, F. & Denk, W. Deep tissue two-photon microscopy. *Nat. Methods* **2**, 932–940 (2005).
4. Prevedel, R. et al. Fast volumetric calcium imaging across multiple cortical layers using sculpted light. *Nat. Methods* **13**, 1021–1028 (2016).
5. Grewe, B. F., Voigt, F. F., van't Hoff, M. & Helmchen, F. Fast two-layer two-photon imaging of neuronal cell populations using an electrically tunable lens. *Biomed. Opt. Express* **2**, 2035–2046 (2011).
6. Shain, W. J., Vickers, N. A., Goldberg, B. B., Bifano, T. & Mertz, J. Extended depth-of-field microscopy with a high-speed deformable mirror. *Opt. Lett.* **42**, 995 (2017).
7. Sofroniew, N. J., Flickinger, D., King, J. & Svoboda, K. A large field of view two-photon mesoscope with subcellular resolution for in vivo imaging. *eLife* **5**, e14472 (2016).
8. Kong, L. et al. Continuous volumetric imaging via an optical phase-locked ultrasound lens. *Nat. Methods* **12**, 759–762 (2015).
9. Yang, W. et al. Simultaneous multi-plane imaging of neural circuits. *Neuron* **89**, 269–284 (2015).
10. Lu, R. et al. Video-rate volumetric functional imaging of the brain at synaptic resolution. *Nat. Neurosci.* **20**, 620 (2017).
11. Song, A. et al. Volumetric two-photon imaging of neurons using stereoscopy (vTwINS). *Nat. Meth* **14**, 420–426 (2017).
12. Hoover, E. E. et al. Remote focusing for programmable multi-layer differential multiphoton microscopy. *Biomed. Opt. Express* **2**, 113 (2011).
13. Cheng, A., Gonçalves, J. T., Golshani, P., Arisaka, K. & Portera-Cailliau, C. Simultaneous two-photon calcium imaging at different depths with spatiotemporal multiplexing. *Nat. Methods* **8**, 139–142 (2011).
14. Chen, J. L., Voigt, F. F., Javadzadeh, M., Krueppel, R. & Helmchen, F. Long-range population dynamics of anatomically defined neocortical networks. *eLife* **5**, e14679 (2016).
15. Stirman, J. N., Smith, I. T., Kudenov, M. W. & Smith, S. L. Wide field-of-view, multi-region, two-photon imaging of neuronal activity in the mammalian brain. *Nat. Biotechnol.* **34**, 857–862 (2016).
16. Weisenburger, S. et al. Volumetric Ca^{2+} imaging in the mouse brain using hybrid multiplexed sculpted light microscopy. *Cell* **170**, 1050–1066 (2019).
17. Wu, J. et al. Kilohertz in vivo imaging of neural activity. Preprint at https://doi.org/10.1101/543058 (2019).
18. Heshmat, B., Tancik, M., Satat, G. & Raskar, R. Photography optics in the time dimension. *Nat. Photonics* **12**, 560–566 (2018).
19. Beaurepaire, E., Oheim, M. & Mertz, J. Ultra-deep two-photon fluorescence excitation in turbid media. *Opt. Commun.* **188**, 25–29 (2001).
20. Horton, N. G. et al. In vivo three-photon microscopy of subcortical structures within an intact mouse brain. *Nat. Photonics* **7**, 205–209 (2013).

Methods

Microscope system. The laser used was a Coherent Chameleon Ultra II laser (3.5 W tunable Ti:Sapphire, 80 MHz repetition rate) with pulse rate reduced to 20 MHz by a Conoptics pulse picker (Model 350-210-RA). The laser was typically operated around 930 nm wavelength. Beam steering was performed with a Thorlabs LSK-GR08 galvo-resonant scan head, and *z*-scanning was provided by a Thorlabs MZS500 piezo stage. The objective was a Nikon CFI75 LWD 16× with a numerical aperture of 0.8. Detection was performed by a Hamamatsu H7422PA-40 photomultiplier tube, amplified by a Femto HCA-400M-5K-C. Readout was performed by a National Instruments 5771 digitizer and 7972 FPGA combination using customized Vidrio ScanImage software. An Analog Devices AD9516 was used to synchronize the digitizer sampling to the laser pulses. The instrument response time of our detection electronics was confirmed to be better than a nanosecond, as inferred from the signal produced by a second-harmonic crystal sample.

Animal surgery and in vivo imaging. All animal procedures were approved by the Boston University Institutional Animal Care and Use Committee and carried out in accordance with NIH standards.

Acute preparations. Mice were anesthetized with ketamine–xylazine, the skin over the mouse dorsal cranium was retracted and sterile surgical procedures were used to replace a small portion of the skull over the olfactory bulb or dorsal neocortex with imaging windows composed of a 4 -mm glass coverslip[21]. Imaging windows and a stainless-steel head post were both anchored with dental acrylic (Metabond, Parkell). Mice were maintained under ketamine–xylazine anesthesia, held in a stereotaxic apparatus and imaged immediately following surgery. Fluorescent vascular labeling was performed using retroorbital injection of dextran-conjugated FITC (2 MDa, 60 µl of 5% w/v in sterile PBS; Sigma-Aldrich). Neural labeling in the olfactory bulb was accomplished by crossing a Cre-expressing driver line (Tbet-Cre[22]) with a conditional reporter (line Ai148 (ref. [23])), which selectively labeled second-order projection neurons. Sensory responses were driven by odors delivered by driving pressurized air through the headspace of vials containing odorants diluted at 2–5% vol/vol (ethyl tiglate, 2-hexanone and amyl acetate), and directing it to the animal's nose using silicone tubing and a custom nose cone.

Chronic preparations. A chronic cranial window surgery was performed on a female C57Bl6-GCaMP6s mouse (15 weeks old, The Jackson Laboratory). The surgical procedure was modified from the procedure previously described in reference[24]. The left somatosensory cortex was exposed over a 4-mm-diameter circular area, with the center positioned 2.5 mm posteriorly and 2.5 mm laterally to bregma and sealed with a coverslip (Warner Instruments, 64–0724) using dental acrylic. A metal head post, used for immobilization of the head during imaging, was glued to the bone contralateral to the glass implant. A well was created using dental acrylic and a 3D-printed custom ring to hold the water required for the objective immersion. The animal was then left to recover for 1 week before training for head-fixed awake imaging, for up to 1.5 h on a custom hammock. The animal was given sweetened condensed milk during the training and every 15 min during imaging sessions.

Data analysis. For analysis of coding and odor tuning, each stimulus was presented for 3 s, and this was repeated 3 times in interleaved order. Image time series were analyzed separately for each individual plane. Motion correction was applied in some cases to offset movement from respiration (Turboreg plugin in ImageJ). Regions of interest (ROIs) encompassing glomeruli and mitral/tufted somata were manually identified in ImageJ on the basis of average intensity images collapsed across the entire time series. The mean fluorescence intensity F_0 was measured for each ROI throughout the trial period and converted to $\Delta F/F$ by dividing by the mean of the 50 frames (~1.5 s) immediately preceding odor presentation. $\Delta F/F$ traces were averaged across all trials for each odor and plotted as heat maps. Sensory tuning was assessed on the basis of the mean response strength for each odorant, calculated as the mean of the response from 0.5 s to 2.0 s during the 3-s odor presentation.

Photodamage assessment. We probed for potential photodamage by continuously imaging the mouse olfactory bulb for a period of o more than 1 h, applying 3 times the laser power used in experiments measuring sensory responses (achieved by not pulse-picking the laser beam). Continuous imaging was interspersed with brief 20-s odor stimulation trials, in which we probed for changes in the amplitude of sensory responses or resting fluorescence levels. We quantified responses to 2 different odors across 15 different ROIs identified as having robust sensory-driven activity. This resulted in no perceptible degradation in the neuronal odor responses, as characterized by F_0, ΔF and $\Delta F/F$ (Supplementary Note 1).

Data illustrating the lack of photobleaching are shown for one representative animal. Photostability was assessed using $n = 15$ glomeruli, each quantified by peak amplitude normalized to the size of the first response. GCaMP signals were quantified based on ROIs encompassing glomerular neuropil or mitral/tufted cell somata as appropriate, and were quantified as mean values for each ROI. Response strength was calculated as peak responses during the 90 image frames during the 3-second odor presentation, relative to the 50 image frames immediately prior.

Reporting Summary. Further information on research design is available in the Nature Research Reporting Summary linked to this article.

Data availability

The data that support the plots within this paper and other findings of this study are available from the corresponding authors upon reasonable request.

Code availability

The code that support the plots within this paper and other findings of this study are available from the corresponding authors upon reasonable request.

References

21. Holtmaat, A. et al. Long-term, high-resolution imaging in the mouse neocortex through a chronic cranial window. *Nat. Protoc.* **4**, 1128–1144 (2009).
22. Isogai, Y. et al. Molecular organization of vomeronasal chemoreception. *Nature* **478**, 241–245 (2011).
23. DaigleT. Let al.A suite of transgenic driver and reporter mouse lines with enhanced brain-cell-type targeting and functionality. *Cell* **174**, 465–480 (2018).
24. Uhlirova, H. et al. Cell type specificity of neurovascular coupling in cerebral cortex. *eLife* **5**, e14315 (2016).

Acknowledgements

We thank H. Li for initial help in the construction of our reverberation microscope, and the Boston University Neurophotonics Center and B. S. Lee for help with animal preparations. This work was supported in part by the Engineering Research Centers Program of the National Science Foundation under NSF cooperative agreement no. EEC-1647837.

Author contributions

J.M. and D.B. conceived the reverberation technique, with T.G.B.'s help. D.B. developed and implemented the prototype microscope. I.D. and K.K. provided the mouse subjects. D.B., I.D. and J.M. analyzed the data. All authors contributed to experiments and the writing of the manuscript.

Competing interests

D.R.B., T.G.B., and J.M. are co-inventors on provisional patent application 62/697,662 submitted by Boston University, that covers 'Reverberation Microscopy Systems and Methods'. T.G.B. acknowledges a financial interest in Boston Micromachines Corporation (BMC), which manufactures components sometimes used in multiphoton microscopy. However, no BMC products were used in the work described in this paper.

Additional information

Supplementary information is available for this paper at https://doi.org/10.1038/s41592-019-0728-9.

Correspondence and requests for materials should be addressed to D.R.B.

Peer review information Rita Strack was the primary editor on this article and managed its editorial process and peer review in collaboration with the rest of the editorial team.

Reprints and permissions information is available at www.nature.com/reprints.

nature research

Corresponding author(s): Devin R. Beaulieu

Last updated by author(s): 6 December 2019

Reporting Summary

Nature Research wishes to improve the reproducibility of the work that we publish. This form provides structure for consistency and transparency in reporting. For further information on Nature Research policies, see Authors & Referees and the Editorial Policy Checklist.

Statistics

For all statistical analyses, confirm that the following items are present in the figure legend, table legend, main text, or Methods section.

n/a	Confirmed	
☐	☒	The exact sample size (*n*) for each experimental group/condition, given as a discrete number and unit of measurement
☐	☒	A statement on whether measurements were taken from distinct samples or whether the same sample was measured repeatedly
☐	☒	The statistical test(s) used AND whether they are one- or two-sided *Only common tests should be described solely by name; describe more complex techniques in the Methods section.*
☒	☐	A description of all covariates tested
☒	☐	A description of any assumptions or corrections, such as tests of normality and adjustment for multiple comparisons
☐	☒	A full description of the statistical parameters including central tendency (e.g. means) or other basic estimates (e.g. regression coefficient) AND variation (e.g. standard deviation) or associated estimates of uncertainty (e.g. confidence intervals)
☐	☒	For null hypothesis testing, the test statistic (e.g. *F*, *t*, *r*) with confidence intervals, effect sizes, degrees of freedom and *P* value noted *Give P values as exact values whenever suitable.*
☒	☐	For Bayesian analysis, information on the choice of priors and Markov chain Monte Carlo settings
☒	☐	For hierarchical and complex designs, identification of the appropriate level for tests and full reporting of outcomes
☒	☐	Estimates of effect sizes (e.g. Cohen's *d*, Pearson's *r*), indicating how they were calculated

Our web collection on statistics for biologists contains articles on many of the points above.

Software and code

Policy information about availability of computer code

Data collection	ScanImage (Custom Version), MATLAB (2018b)
Data analysis	MATLAB (2019b), ImageJ (2.0.0-rc-69/1.52)

For manuscripts utilizing custom algorithms or software that are central to the research but not yet described in published literature, software must be made available to editors/reviewers. We strongly encourage code deposition in a community repository (e.g. GitHub). See the Nature Research guidelines for submitting code & software for further information.

Data

Policy information about availability of data

All manuscripts must include a data availability statement. This statement should provide the following information, where applicable:

- Accession codes, unique identifiers, or web links for publicly available datasets
- A list of figures that have associated raw data
- A description of any restrictions on data availability

The data that support the findings of this study are available from the corresponding author upon reasonable request.

Field-specific reporting

Please select the one below that is the best fit for your research. If you are not sure, read the appropriate sections before making your selection.

☒ Life sciences ☐ Behavioural & social sciences ☐ Ecological, evolutionary & environmental sciences

For a reference copy of the document with all sections, see nature.com/documents/nr-reporting-summary-flat.pdf

Life sciences study design

All studies must disclose on these points even when the disclosure is negative.

Sample size	Three different structures with various contrast. One sample (mouse) each for vasculature and neocortex experiments. Two samples (mice) for the olfactory bulb experiment. We believe this was sufficient to demonstrate the technique.
Data exclusions	Multiple images were taken of each animal, with the best of each selected for inclusion in the paper; this was pre-established. No data was excluded from statistical results.
Replication	Experiments were successfully replicated on multiple different animals, fluorophores, and brain structures. The culminating olfactory bulb experiments were repeated on two mice with comparable results.
Randomization	Randomization was not relevant as there were no groups used in the experiments.
Blinding	Blinding was not relevant as there were no groups used in the experiments.

Reporting for specific materials, systems and methods

We require information from authors about some types of materials, experimental systems and methods used in many studies. Here, indicate whether each material, system or method listed is relevant to your study. If you are not sure if a list item applies to your research, read the appropriate section before selecting a response.

Materials & experimental systems

n/a	Involved in the study
☒	☐ Antibodies
☒	☐ Eukaryotic cell lines
☒	☐ Palaeontology
☐	☒ Animals and other organisms
☒	☐ Human research participants
☒	☐ Clinical data

Methods

n/a	Involved in the study
☒	☐ ChIP-seq
☒	☐ Flow cytometry
☒	☐ MRI-based neuroimaging

Animals and other organisms

Policy information about studies involving animals; ARRIVE guidelines recommended for reporting animal research

Laboratory animals	Mouse; 3-6 months of age; C57Bl6/J, Tbet-Cre::Ai148 (Male; JAX #'s 024507, 030328) and Thy1-GCaMP6s (Female)
Wild animals	The study did not involve wild animals.
Field-collected samples	The study did not include samples collected from the field.
Ethics oversight	All procedures were approved by the Boston University Institutional Animal Care and Use Committee.

Note that full information on the approval of the study protocol must also be provided in the manuscript.